chemosensors

MDPI

Article

TiO_2 Ceramic Nanotubes—Conducting Polymer Assemblies with Embedded Gold Particles for Potential Use as Chemosensors in the Detection of Oral Diseases

Oliver Daniel Schreiner [1,2], Alexandru F. Trandabat [1], Romeo Cristian Ciobanu [1,*] and Thomas Gabriel Schreiner [2]

[1] Department of Electrical Measurements and Materials, Gheorghe Asachi Technical University, 700050 Iasi, Romania; oliver090598@yahoo.com (O.D.S.); ftranda@tuiasi.ro (A.F.T.)
[2] Department of Medical Specialties III, Faculty of Medicine, University of Medicine and Pharmacy "Grigore T. Popa", 700115 Iasi, Romania
* Correspondence: r.c.ciobanu@tuiasi.ro

Abstract: Our research outlines a method for creating chemosensors utilizing hybrid nanostructures derived from TiO_2 ceramic nanotubes alongside conducting polymers, with embedded gold nanoparticles. The method used to create hybrid nanostructures from ceramic nanotubes and conducting polymers was drop-casting. AFM analysis highlighted an increased roughness, particularly for PANI-EB, exhibiting a significantly larger grain size exceeding 3.5 µm, with an increased inclusion of gold and uniform arrangement on the surface. The Rku parameter values being around three suggested that the layers primarily exhibited peaks rather than depressions, showing a Gaussian distribution. A chemiresistor was created by using an ink-jet printer and a multilayer metallization was achieved with commercial silver ink for printed electronics. Based on the experimental calibration curve, which exhibits adequate linearity over a wider range of H_2S concentrations in air up to 1 ppm, the detection limit was established at 0.1 ppm, a threshold appropriate for recognizing oral diseases. The sensor is a simple, affordable, and durable device designed for individual use, offering significant benefits for patients by enabling improved tracking of the syndrome's advancement or treatment success.

Keywords: ceramic nanotubes; conducting polymers; gold nanoparticles; chemosensor; oral diseases

check for updates

Received: 23 February 2025
Revised: 17 March 2025
Accepted: 19 March 2025
Published: 22 March 2025

Citation: Schreiner, O.D.; Trandabat, A.F.; Ciobanu, R.C.; Schreiner, T.G. TiO_2 Ceramic Nanotubes—Conducting Polymer Assemblies with Embedded Gold Particles for Potential Use as Chemosensors in the Detection of Oral Diseases. *Chemosensors* **2025**, *13*, 117. https://doi.org/10.3390/chemosensors13040117

Copyright: © 2025 by the authors. Licensee MDPI, Basel, Switzerland. This article is an open access article distributed under the terms and conditions of the Creative Commons Attribution (CC BY) license (https://creativecommons.org/licenses/by/4.0/).

1. Introduction

Oral diseases rank among the most prevalent human ailments, yet they are less researched. These illnesses impact the physical, mental, and social well-being of patients, leading to diminished quality of life. Inadequate oral care, genetic predispositions, and external influences significantly impact the onset and advancement of these conditions. Despite the existence of treatment alternatives for these conditions, recurrences limit their effectiveness [1]. The result is bad breath, a significant health issue. Despite its significance, patients often fail to notice their own oral malodor, and this challenge can lead to anxiety in those experiencing halitosis [1]. Foul odors arising from the mouth signify the metabolic activity of the entire oral microbial community. The breakdown of sulfur-containing amino acids in the mouth and upper/lower respiratory tract, and their exchange with blood in the alveoli, causes halitosis. Analytical methods relying on organoleptic assessments are essential for quantifying foul-smelling gases in the diagnosis and management of halitosis. However, it is possible that bad-smelling oral gases signify not just halitosis but also the pathogenic potential of oral microbiota.

Human breath that is exhaled includes nitrogen (approximately 78%), oxygen (16%), carbon dioxide (4–5%), hydrogen (5%), and water vapor. Oral volatile sulfur compounds (VSCs) are significantly generated in the oral cavity due to bacterial activity, stemming from the decomposition of sulfur-containing amino acids. Hydrogen sulfide (H_2S), methyl mercaptan (CH_3SH), and, to a smaller degree, dimethyl sulfide account for 90% of the VSCs associated with halitosis. H_2S is a gaseous neurotransmitter, mainly generated internally, which plays a role in the control of cellular functions. A significant rise in H_2S levels suggests the existence of different oral diseases in the individual [2].

Gas chromatography has been utilized to analyze hydrogen sulfide and methyl mercaptan, which are representative VSCs; however, this method is costly and necessitates skilled operators [3]. The VSC cut-off thresholds for identifying halitosis were determined by gas chromatography to be 65.79 ppb for females and 79.94 ppb for males, though these figures pertain to the group of individuals included in a specific clinical study [4]. Typically, any concentration exceeding 0.5 ppm is regarded as significant for the diagnosis of halitosis and associated metabolic issues [5], irrespective of the measurement technique employed [6]. Portable gas chromatography devices like Oral Chroma™ [7] can measure the levels of hydrogen sulfide, methyl mercaptan, and dimethyl sulfide separately. A portable sulfide detector like the Halimeter [8] is specifically designed to assess the overall concentration of sulfide. However, it requires a considerable amount of time for measurement and is exclusively fit for clinical use, despite it providing several clear benefits (portable, user-friendly, reproducible, and providing immediate outcomes). Conversely, it does not have the ability to distinguish between various sulfuric compounds when affected by non-sulfuric volatile substances, like Oral Chroma™ does [9]. Finally, the OralChroma™ device now merges gas chromatography with a gas sensor made of an indium oxide semiconductor. Another similar example is given in [10]. Such combined methods can determine the exact concentrations of each VSC component in 10 min, which is a practical duration for medical applications, but their cost remains fairly high. Lastly, Breathtron® [11] utilizes a semiconductor sensor made of a zinc oxide membrane that is responsive to VSCs. Its assessment is regarded as more precise than that of the Halimeter; however, it requires a lengthy measurement time and is applicable solely in clinical settings.

It is clear, however, that the practical aim of a sensor for oral diseases should not solely depend on its availability in a clinic, but rather the advancement of such sensors should primarily address the requirements of patients who monitor their own conditions. Different kinds of H_2S sensors have been suggested to meet the needs for halitosis investigation [12–14]. The most prevalent H_2S sensors utilize semiconducting metal oxides; they are inexpensive and can be operated quickly and effortlessly [15–19]. Nonetheless, metal oxide semiconductor (MOS) gas sensors generally exhibit low selectivity, since they respond to all reducing or oxidizing gases. Electrochemical sensors were tested as well; however, they are not as sensitive as MOS gas sensors and are affected by variations in temperature and humidity [20]. Various other H_2S-sensing technologies have been suggested, including colorimetric sensors [21], surface acoustic wave gas sensors [22,23], and devices created with different sensing structures based on thick metal oxides [24–27]. Nonetheless, these sensors face challenges linked to the need for selectivity or detection of ppb levels.

Embellishing sensorial frameworks with conductive substances, like graphene, carbon nanotubes (CNTs), or metallic nanoparticles has been widely discussed recently in the literature to improve sensor selectivity, and may be applied in H_2S detection applications. Combining metal oxides with various metal-based catalysts can enhance both sensitivity and selectivity. Certain doped metal oxides may interact with gases that contain sulfur, causing a modification in their electrical conductivity [28–31]. Recent research upon the chemisorption of H_2S on gold nano-structures [32] resulted in sensors exhibiting minimal

variability, excellent selectivity, and enduring stability, positioning gold nanostructures as a strong candidate for further exploration. The impact of gold nano-structures is enhanced when the metal oxide base, where the gold particles are incorporated, is presented as nanowires or nano-sheets. Even though the nanofiber interacted with sulfur-based gases, the incorporation of metal increased its sensitivity to hydrogen sulfide [33–36]. Nevertheless, the complex nature of these processes impeded the production of H_2S sensors with reliable and repeatable attributes. On the other hand, because human exhaled breath contains substantial amounts of water vapor, there are considerable disadvantages for sensors lacking proper moisture resistance, a critical factor to consider alongside the impact of other gases released in human breath [37–39].

In conclusion, to our knowledge, an H_2S sensor that possesses high selectivity, detection capabilities at parts per billion levels, and a straightforward fabrication method resulting in consistent sensor properties has yet to be created, warranting further research in this area. The novelty of this paper mainly relates to the development of hybrid nanostructures formed from TiO_2 nanotubes and conductive polymers doped with gold nanoparticles, exhibiting unique sensing properties that are not present in the current literature. The choice of titanium dioxide is due to its properties as a wide-bandgap semiconductor that exhibits excellent chemical stability and remarkable resistance to corrosion from sulfur-bearing gases. The sensor principle described in the paper is less complex, more cost-effective, and more effective than the methods currently suggested for detecting sulfur-containing gases in breath, akin to the application with the previously mentioned sensor types.

2. Technology for Obtaining Hybrid Nanostructures from Ceramic Nanotubes and Conducting Polymers with Embedded Gold Nanoparticles

Materials and Methods of Preparation

According to the comprehensive technological stages widely described in [40,41], the process for producing ceramic nanotubes involved three steps: creating polymer fiber networks using poly(methyl methacrylate), depositing ceramic coatings onto the nanofiber networks through magnetron deposition, and heating the nanotubes to 600 °C to completely remove the polymer support. The optimal results were achieved with a 10% PMMA solution at 20 kV, with a drum rotation speed of 5 rpm, as the fiber nets exhibited greater homogeneity in both spatial deposition and diameter. Conversely, considering the properties of ceramic thin films to be applied on PMMA nanofibers, a minimum diameter of 0.3 μm was deemed ideal for PMMA nanofibers to ensure the structural stability of coated fibers from a mechanical perspective [41]. Concerning RF magnetron sputtering, ceramic targets measuring 2 inches in diameter and 0.125 inches in thickness were utilized during the deposition process. The deposition time lasted for 1 h, and the RF power supplied to the magnetron was 200 watts.

The process for subsequently obtaining hybrid nanostructures from TiO_2 nanotubes and conductive polymers such as poly(3-hexylthiophene) (P3HT), polyaniline emeraldine-base (PANI-EB), and poly(3, 4-ethylenedioxythiophene)-polystyrene sulfonate (PEDOT-PS) included drop-casting. Five samples of each type were created to evaluate technological feasibility. The technological process involved the use of the solutions outlined in [42]. In all instances, 240 μL of every polymer solution was applied onto ceramic nanotubes (SiO_2/Si substrate) using Pasteur pipettes. Each solvent underwent evaporation for 60 min in a vacuum, using a Pfeiffer vacuum pump linked to a desiccator.

The TiO_2-conductive polymer composite materials were further immersed in a diluted $HAuCl_4$/2-propanol solution (0.001 M) using the dip-coating technique, and stored for 24 h. Following impregnation, the samples were subjected to drying in an oven at 150 °C with a flow of Ar (100 sccm) for 30 min. The samples were subsequently cooled to room temperature in an argon stream. Au nanoparticles with an average size of 100 nm were quasi-uniformly integrated into the hybrid structures. This method for acquiring predefined Au nanoparticles from a highly diluted HAuCl4 solution on the polymer substrate, heated from ambient temperature to just over one hundred degrees Celsius, resembles those described in [43,44]. However, this method, presented in the paper, involves immersing the polymer film in a highly diluted $HAuCl_4$ solution, which has the benefit of forming and quasi-uniformly distributing gold nanoparticles over larger areas, a necessary requirement for creating more responsive gas sensors.

3. Results and Discussion

3.1. Characterization Equipment

Transmission electron microscopy (TEM) results were obtained using a JEOL 2100 Plus transmission electron microscope operating at an accelerating voltage of 80 kV (JEOL Ltd., Akishima, Tokyo, Japan). SAED assessment was carried out as well.

Raman Spectroscopy was performed using AvaRaman 532 instruments (Avantes B.V., Apeldoorn, The Netherlands).

Fourier transform infrared spectroscopy (FTIR) was performed using JASCO instruments (Tokyo, Japan), across a spectral range of 12,000–50 cm^{-1}.

X-ray photoelectron spectroscopy (XPS) and energy-dispersive X-ray spectroscopy (EDS) were performed utilizing an AXIS Supra+ system (Kratos Analytical Ltd., Manchester, UK).

Scanning electron microscopy (SEM) was performed with Lyra III XMU equipment (TESCAN GROUP a.s., Brno-Kohoutovice, Czech Republic). To evaluate the obtained graphene layer, a sequential morphological examination was performed.

An assessment using atomic force microscopy (AFM) was conducted with a Dimension Edge instrument from Bruker (Billerica, MA, USA) for optical purposes. Average roughness measurements are provided for four scanned regions on each type of sample. The analysis of the surface roughness parameters was according to [45,46].

3.2. TEM and Selected Area (Electron) Diffraction (SAED) Analysis of TiO_2—Conducting Polymers Composites

The TEM images for TiO_2 nanotube composites are presented in Figures 1–3, from which the tetragonal TiO_2 anatase phase can be identified, as nanotubes with diameters of approx. 400–500 nm with extended areas of crystalline coherence. The pick intensity from the EDX spectrum related to the concentration of TiO_2 nanotubes in the composite assembly is similar in all diagrams. But, for each diagram, the other picks beyond Ti are specific to the composition of the respective polymer corresponding to the composite assembly. In Figure 1, from the EDX spectrum, the TiO_2/PANI-EB ratio was 30:70 (% at).

In Figure 2, from the EDX spectrum, the TiO_2/PEDOT:PS ratio was 33.3:66.6 (% at).

In Figure 3, from the EDX spectrum, the TiO_2/P3HT ratio was 28:72 (% at).

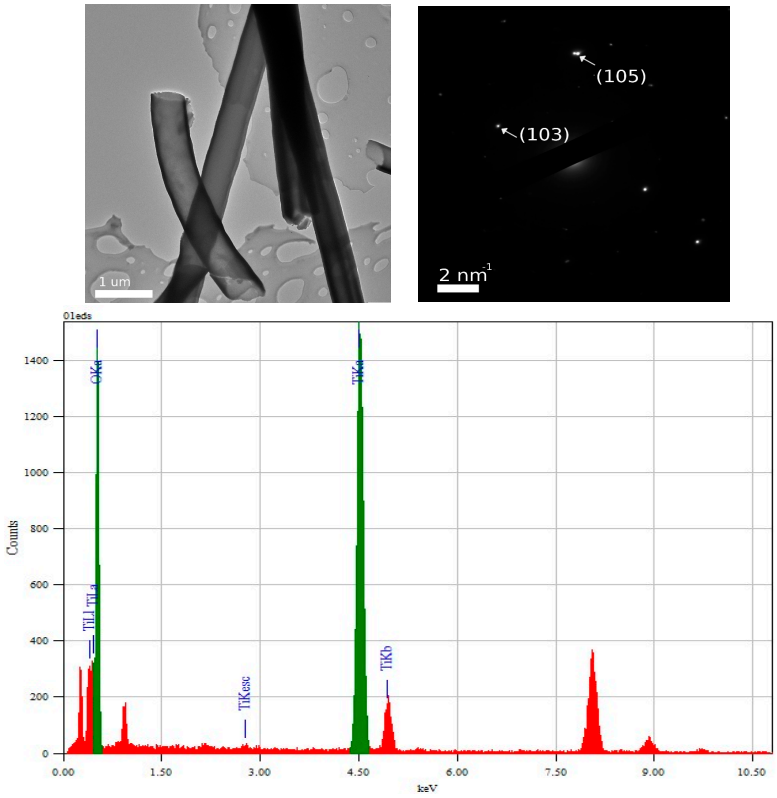


Figure 1. TEM image for TiO_2 nanotube–PANI-EB composite.

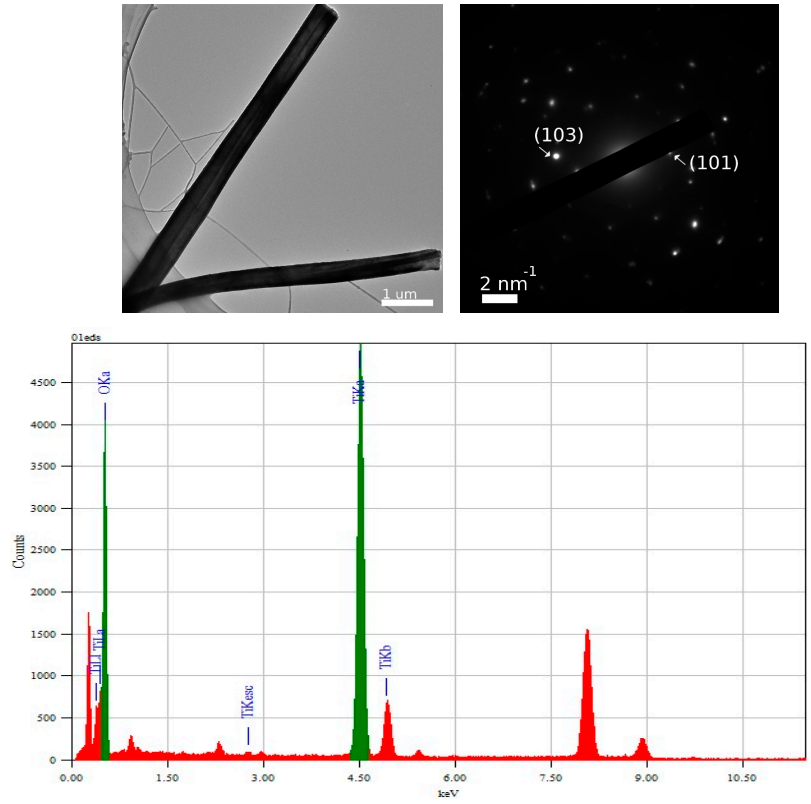


Figure 2. TEM image for TiO_2 nanotube–PEDOT:PS composite.

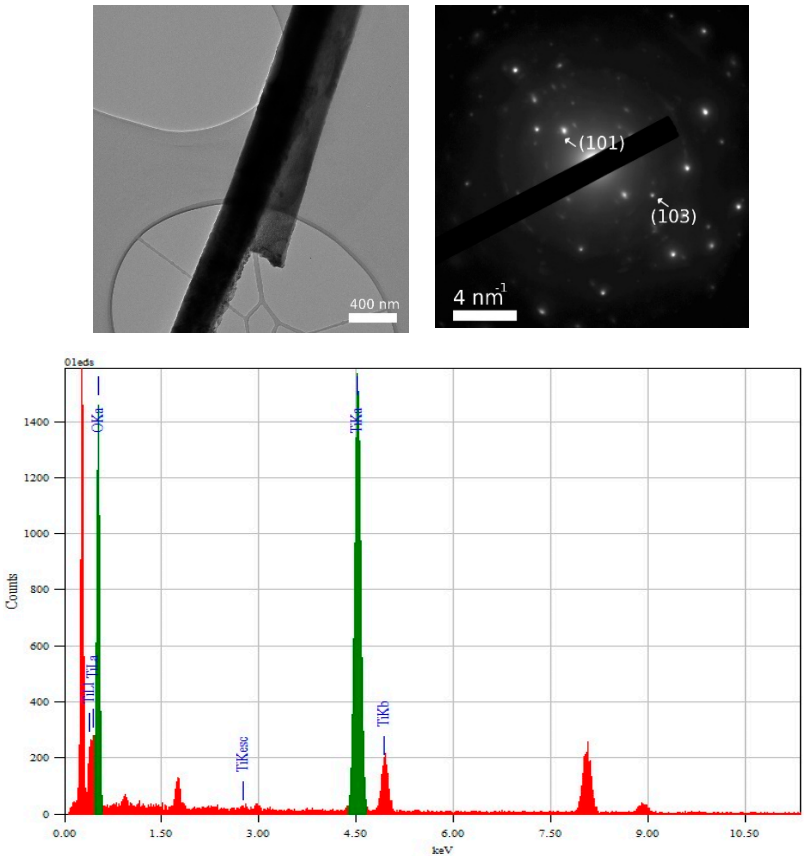


Figure 3. TEM image for TiO_2 nanotube–P3HT composite.

3.3. Raman and FTIR, XPS, and EDS Analysis of TiO_2—Conducting Polymers Composites

Figure 4 shows the Raman spectra recorded at an excitation wavelength of 514 nm for TiO_2 nanotube composites with PANI-EB, PEDOT:PS, and P3HT. The analysis reveals that the main Raman lines of the TiO_2 nanotubes are located at 144, 396, 519, and 639 cm^{-1}, attributed to the Eg, B_1g, A_1g, and Eg vibration modes [47]. In general, for all spectra of TiO_2 nanotube–polymer composites, each Raman spectrum corresponds to the sum of the two constituents of the respective composite materials. The absorption bands of the three polymers may be independently identified: (i) PANI-EB at approx. 814, 1176, 1247, 1352, 1414, 1501, 1565, and 1610 cm^{-1}, attributed to the deformation vibration modes of the benzene ring (B), of the C-H bond in the benzene ring, the C-N stretch, C-H bond in the quinoid ring, C-C stretch in the quinoid ring, and C-H bond in the quinoid ring, the C=N stretch, the C=C stretch in the quinoid ring and, respectively, the C-C stretch in the benzene ring [48]; (ii) PEDOT PS at approx. 439–574–990, 1257, 1364, 1439, 1502, and 1569 cm^{-1} are attributed to the vibrational modes of deformation of the oxyethylene ring, of C_α-$C_{\alpha'}$ stretching and C-H bending, of C_β-$C_{\beta'}$ stretching, of symmetric C-C stretching and of asymmetric C-C stretching [49]; (iii) 729, 1013, 1092, 1184, 1380, 1442, 1515 and 1620 cm^{-1} attributed to C_α-S-$C_{\alpha'}$ bond deformation vibration modes, C_β-C_{alchil} stretching, C_β-H bond bending, C_α-$C_{\alpha'}$ stretching, C_β-H bending, C_β-C_β stretching, C_α=C_β stretching, $C_{\alpha'}$=$C_{\beta'}$ stretching and, respectively, the quinoid structure [50].

The XPS analysis of the TiO_2 nanotube composites is presented in Figure 5. Measurement conditions are as follows: Anode Al (1486.74 eV); U = 15.kV; I = 15 mA; P = 225 W; p SAC 5 X 10–9 mbar; Parameter spectrum recording Line Extended spectrum E start (eV), 1200; Estop (eV), −5; step (eV), 0.1; Pass Energy (eV), 140; number of passes, 1.

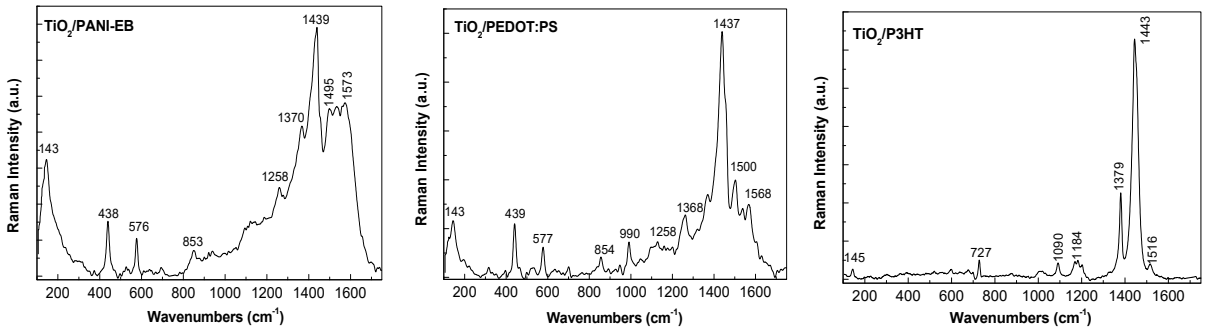


Figure 4. Raman spectra of TiO_2 nanotubes composites with PANI-EB, PEDOT:PS, and P3HT.

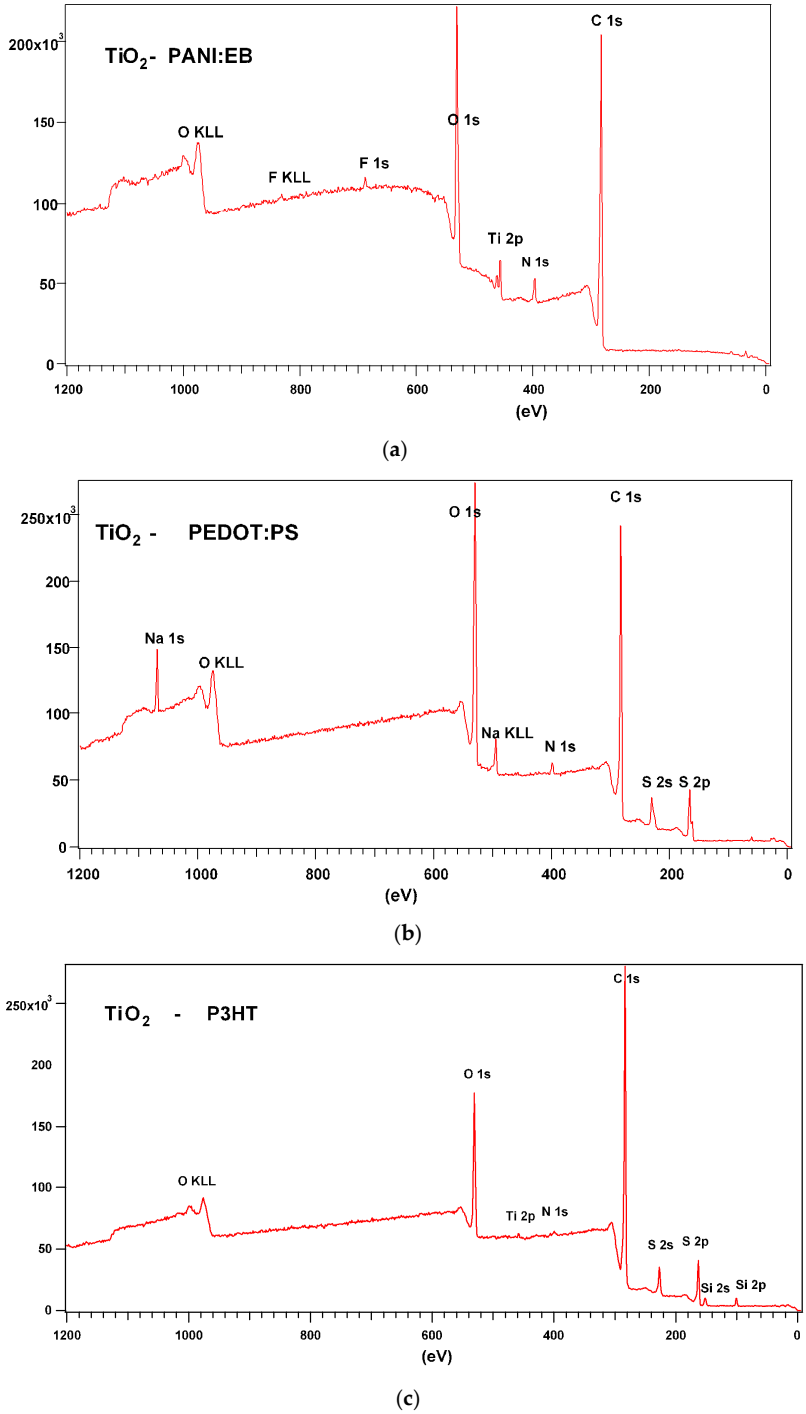


Figure 5. XPS analysis of TiO_2 nanotubes composites with (**a**) PANI-EB, (**b**) PEDOT:PS, and (**c**) P3HT.

In Figure 5a, related to the TiO_2-PANI:EB sample, the identified elements are as follows: fluorine, oxygen, titanium, nitrogen, and carbon, for which high-resolution spectra were recorded (main peaks: F 1s, O 1s, Ti 2p, N 1s, C 1s). In Figure 5b related to the TiO_2-PEDOT:PS sample, the elements present on the surface with main peaks were sodium, oxygen, nitrogen, carbon, and sulfur (Na 1s, O 1s, N 1s, C 1s, S 2p). Finally, in Figure 5c, related to the TiO_2-P3HT sample, the identified elements are as follows: oxygen, titanium, nitrogen, carbon, sulfur, and silicon (main peaks: O 1s, Ti 2p, N 1s, C1s, S 2p and Si 2p).

3.4. SEM Analysis of TiO_2—Conducting Polymers Composites with Au Addition

SEM image 6, of TiO_2/PANI-EB composites with Au, reveals that some gold nanoparticles attach to the TiO_2 nanotubes, while others fit into the gaps between the ceramic nanotubes. The dispersion of gold nanoparticles is quite uniform and the quantity is relevant, although some agglomerations are observable.

From SEM image 7, of TiO_2/PEDOT: PS composites with Au, it can be seen that gold was rarely deposited in the form of nanoparticles, but rather in the form of clusters. It seems that the area covered in gold seems to be reduced.

From SEM image 8 of TiO_2/P3HT composites with Au, it can be seen that gold was primarily deposited in the form of nanoparticles, but some forms of clusters are also visible. The morphology is similar to TiO_2/PANI-EB composites with Au; however, the area coated in gold appears to be slightly diminished.

3.5. AFM Analysis of TiO_2—Conducting Polymers Composites with Au Addition

Figures 6–8 emphasize the surface analysis via SEM. It is evident that the gold was deposited both in the form of nanoparticles and in clusters, influenced by the affinity to the polymer used for deposition support, but also related to the spatial architecture of TiO_2—conducting polymer composites before being submitted to the dip-coating technique, consistent with the findings shown in [42] for different ceramic nanotubes, yet utilizing the same polymers.

From an optical perspective, Figures 9–11 resulted in comparable conclusions to Figures 6–8, noting that the sample includes both TiO_2 nanotubes and Au.

It should be noted that the composite films exhibit varying thicknesses, and although uniform films were achieved for all polymer cases, more uniform structures were associated with the composite containing PEDOT-PS and PANI-EB, where it seems that the polymer was deposited more effectively, and covered, much more efficiently, the spaces formed between the nanotubes.

Additionally, the AFM optical examination displayed the grain size, their distribution across the surface, and the overall roughness of the surfaces [45,46].

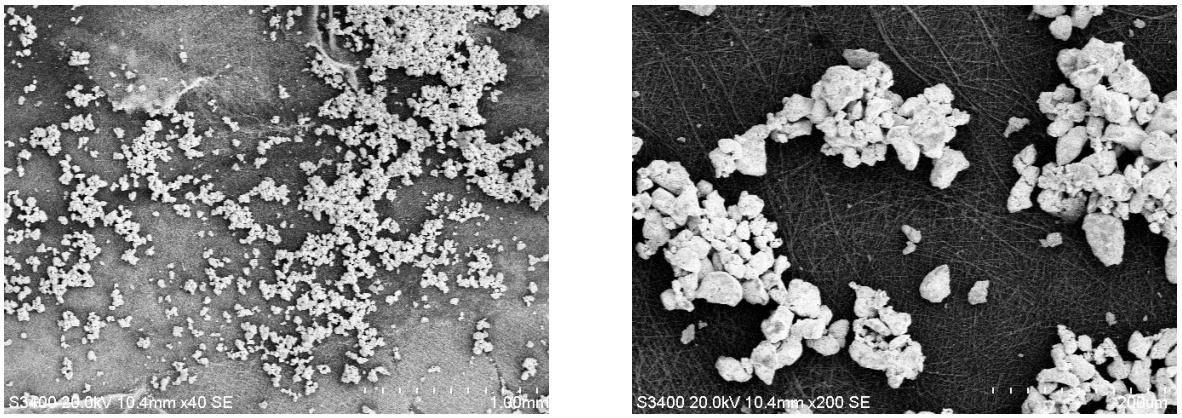


Figure 6. SEM image of TiO_2/PANI-EB composites with Au.

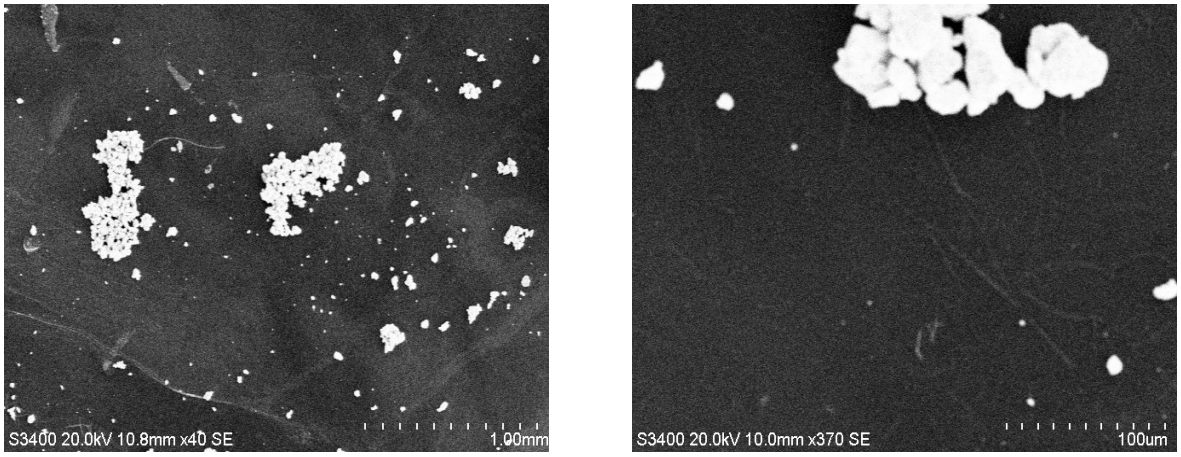


Figure 7. SEM image of TiO_2/PEDOT: PS composites with Au.

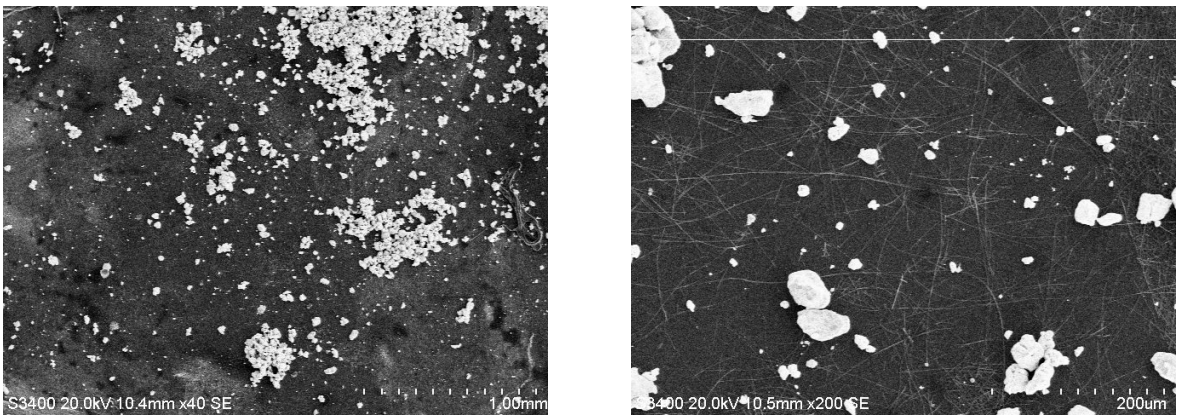


Figure 8. SEM image of TiO_2/P3HT composites with Au.

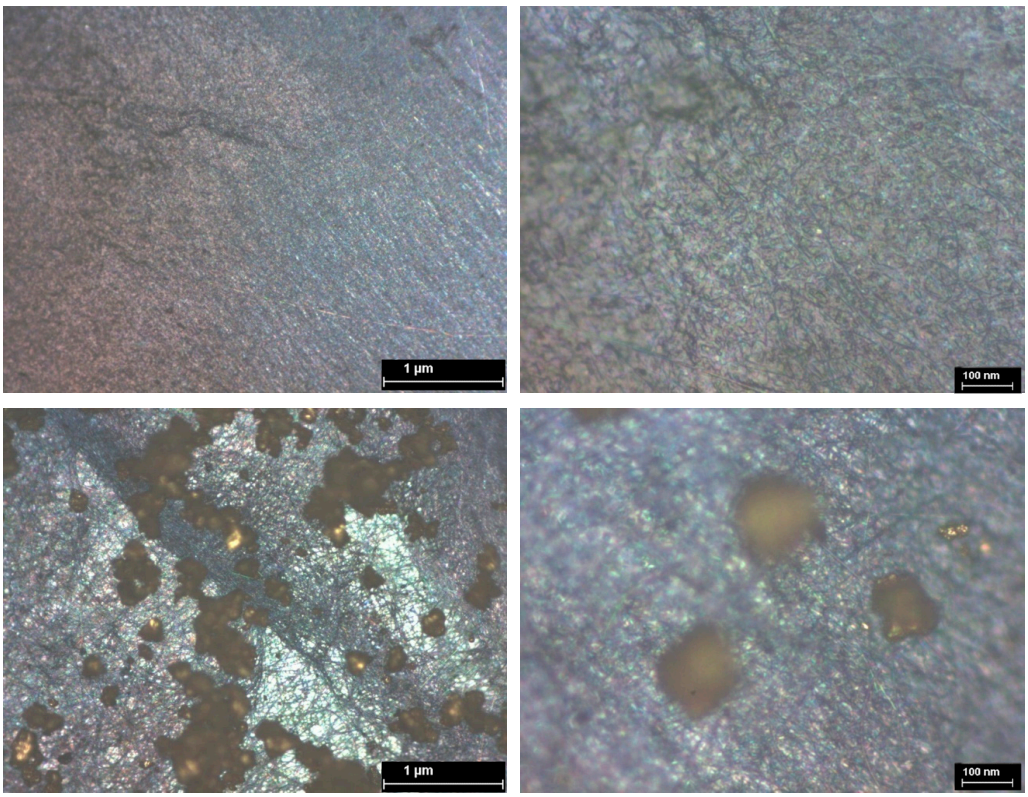


Figure 9. Optical analysis at 100× and 500× of TiO_2/PANI-EB composites without and with Au.

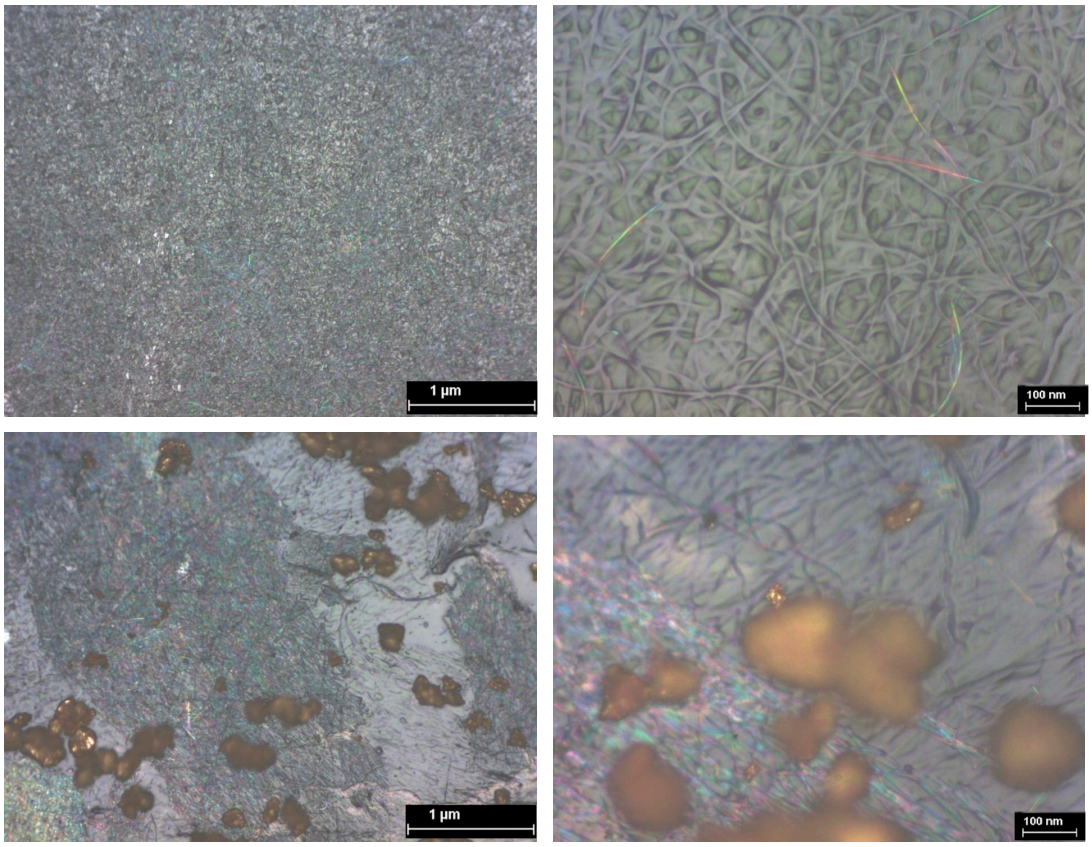


Figure 10. Optical analysis at 100× and 500× of TiO_2/PEDOT: PS composites without and with Au.

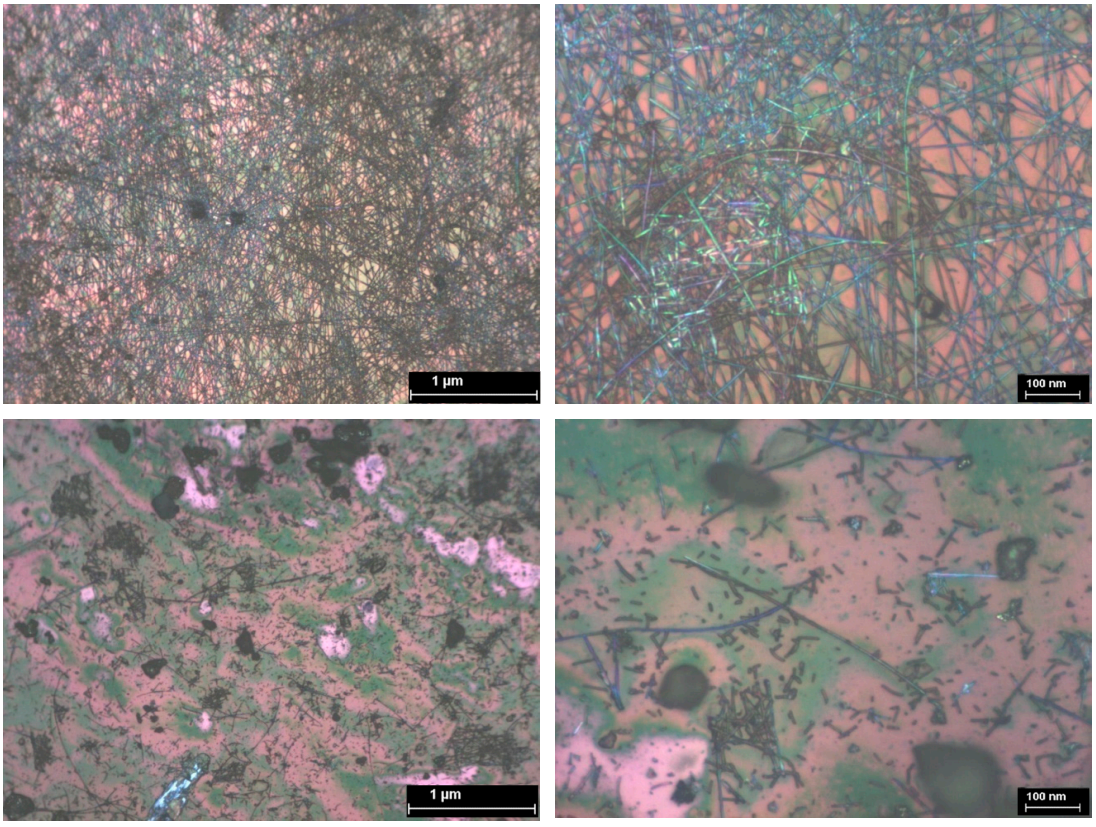


Figure 11. Optical analysis at 100× and 500× of TiO_2/P3HT composites without and with Au.

The results for the roughness parameters determined by AFM lines are comparatively presented in Table 1. In every instance, it was observed that there appears to be a relatively uniform grain distribution; however, the incorporation of gold nanoparticles alters the surface structure and forces the initial grains to create spaces for Au particles to penetrate deeper and accumulate into small clusters, which in turn slightly enhances the grain size and locally sharpens the peaks.

Table 1. Average roughness parameters, determined by AFM lines. Scanned area of 40 × 40 μm.

Scanned Material	RMS (nm)	Ra (nm)	R_{Sk}	R_{Ku}
TiO_2 nanotubes–PANI-EB	947	715	−0.18	4.04
TiO_2 nanotubes–PANI-EB/Au	1197	948	−0.01	2.97
TiO_2 nanotubes–PEDOT: PS	131	105	0.38	3.04
TiO_2 nanotubes–PEDOT: PS/Au	107	79	0.56	4.42
TiO_2 nanotubes–P3HT	362	298	0.17	2.53
TiO_2 nanotubes–P3HT/Au	420	341	0.42	2.89

As regards the profile lines of TiO_2/PANI-EB composites without and with Au, as in Figure 12, the formation of layers is predominantly characterized by peaks and not by depressions; the negative value of Rsk, seen in Table 1, indicates that many low spaces are present on the sample, so we are confronting significant roughness and asymmetry, which are largely mitigated by adding gold nanoparticles, which somewhat organizes the grains into more uniform clusters. This observation is reiterated by the Rku value, which reduces from 4 to about 3, indicating a transition from a random distribution to an almost Gaussian distribution of the grains, confirming that the presence of metal nanoparticles aids in the uniformity of the structure.

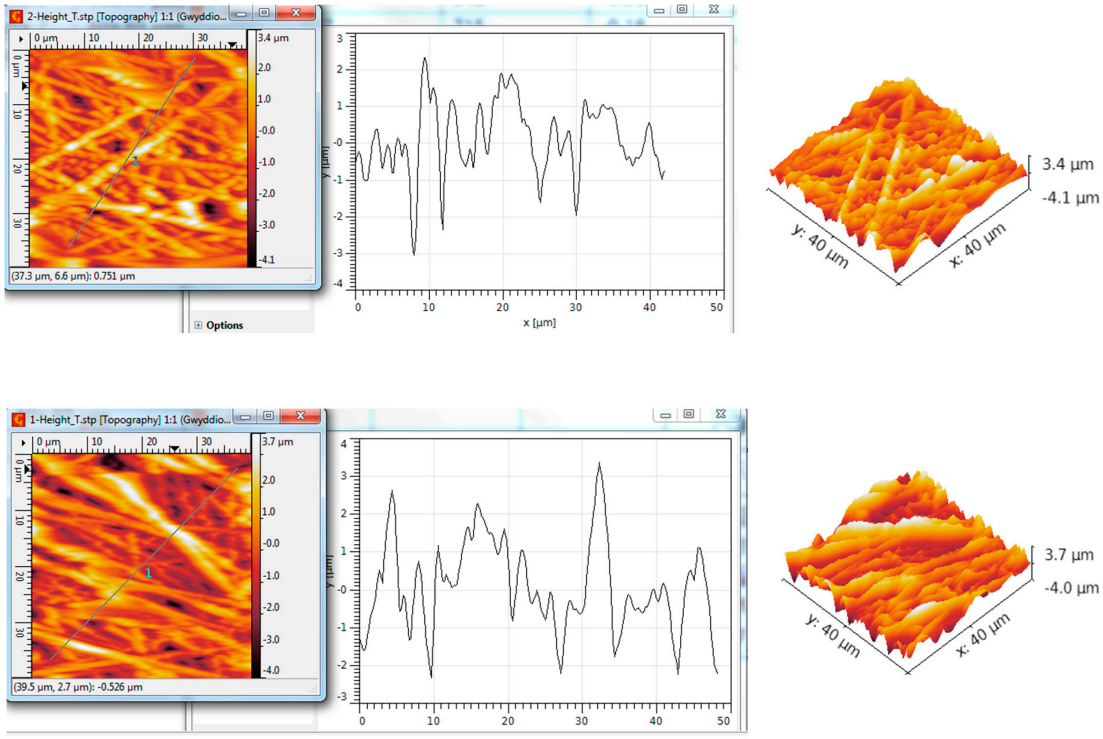


Figure 12. AFM Topographic 2D and 3D images and profile lines, and TiO_2/PANI-EB composites without and with Au.

As regards the profile lines of TiO_2/PEDOT: PS composites without and with Au, Figure 13, the formation of layers is predominantly characterized by large valleys and not by peaks; the presence of gold, predominantly in the form of clusters, explains the increased value of Rsk, suggesting the creation of even broader valleys among the elevated regions. Conversely, the change in symmetry is clear, as the Rku value, originally near three—indicative of a Gaussian distribution—increases beyond four, signifying that the addition of gold nanoparticles as clusters alters the original structure, which was more symmetrical.

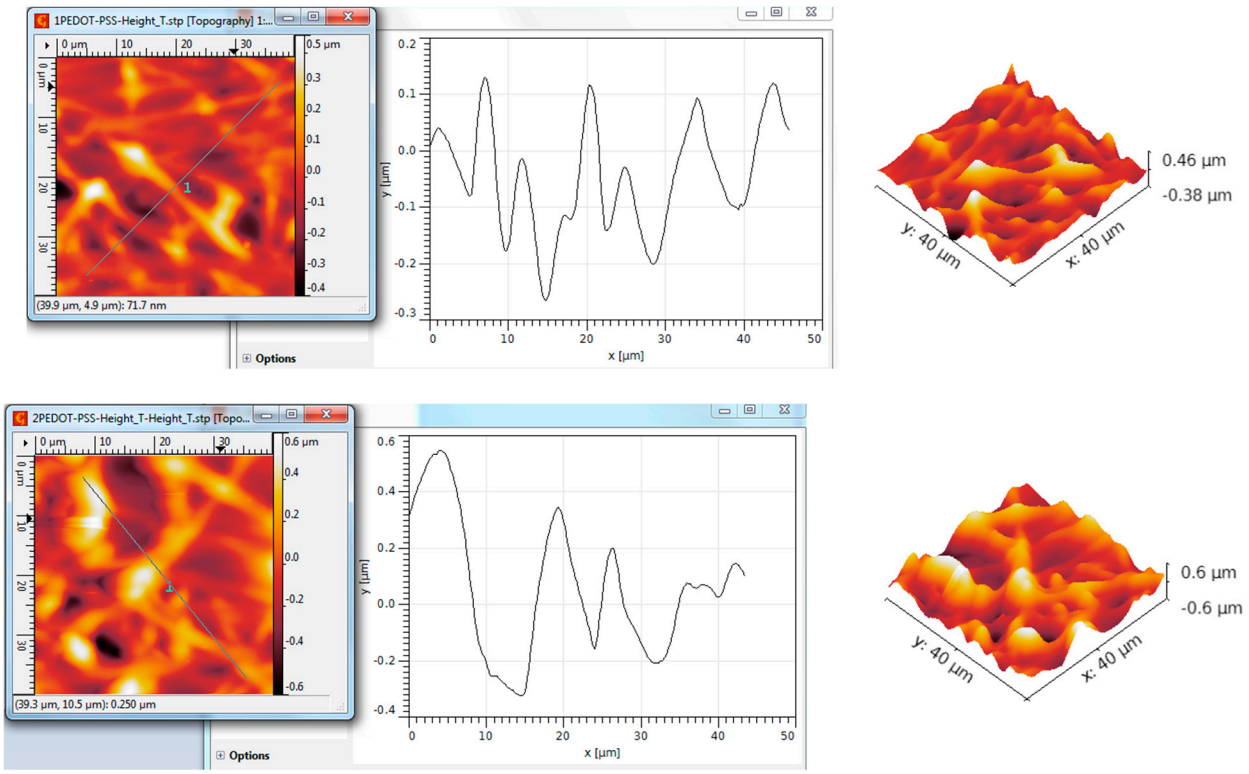


Figure 13. AFM Topographic 2D and 3D images and profile lines, and TiO_2/PEDOT: PS composites without and with Au.

Finally, as regards the profile lines of TiO_2/P3HT composites without and with Au, Figure 14, the grains are generally arranged in smaller clusters in both cases, and the formation of layers is predominantly characterized by peaks and not by depressions. The addition of metal nanoparticles presented a low influence, which confirms the low incorporation observed, e.g., in Figure 11; the Rku values remained near three, indicating that the grain distribution is symmetrical, and slightly more symmetrical in the case of gold incorporation.

Overall, the greatest roughness was obtained from the TiO_2 nanotube structure–PANI-EB with Au, with a much larger grain size dimension of over 3.5 µm, which also exhibits a decent symmetry in the distribution of grains, and greater uniformity in the distribution of polymers within the ceramic nanotubes. At first glance, considering the technical conclusions outlined earlier, this structure, considering the higher incorporation of gold and its distribution on the surface, along with the surface morphology, appears to be the most promising candidate for testing chemisensor properties. Structures exhibiting symmetrical distribution and high roughness dimensions at the µm scale are regarded as optimal for gas sensor applications, because they offer a substantial active area for engagement with the targeted gas. Anatase titanium dioxide experiences a quasi-doping effect when linked with gold nanoparticles, leading to the creation of new energy levels close to the conduction

band, enhancing its sensitivity to sulfur-containing gases; a comparable effect is observed following metal doping for the detection of other gases, as presented in [51–53].

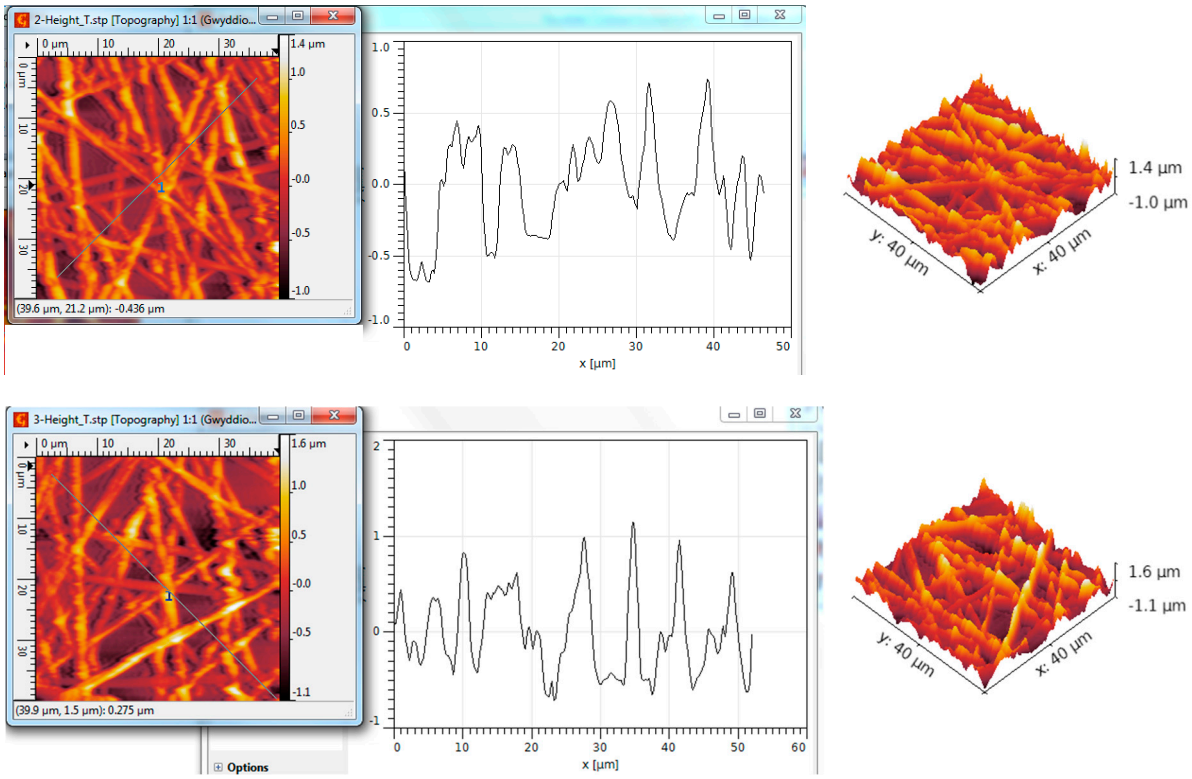


Figure 14. AFM Topographic 2D and 3D images and profile lines, and TiO_2/P3HT composites with Au.

4. Analysis of Functionality as Gas Sensors for H_2s of TiO_2–PANI-EB Composites with the Addition of Gold Nanoparticles

The literature outlines various metallization processes for chemiresistor materials, such as drop-casting, solution electrodeposition, vacuum deposition, and more; however, most of these methods are inappropriate for fundamental sensor applications. In our case, we employed an ink-jet printer to use commercial silver ink for printed electronic applications. A resistor design was developed, showcasing an operational area of roughly 2 cm^2 (a relatively large surface due to the minimal concentration of H_2S that may be exhaled and detected), constrained by two metalized areas forming the conductive connections. The metallization was performed by using commercial ORGACON SI-J20X silver ink (Ag-fa-Gevaert N.V., Mortsel, Belgium) designed for printed electronics, with a multilayer deposition to ensure minimal contact resistance. The design and sensor structure description are presented in Figure 15, with a general design for chemosensors [54].

The performance of the gas sensor was assessed using a testing system similar to the one described in [55]. The sensor was embedded inside a sealed enclosure that allowed gas exchange solely via two valves and access to the electrical connections. An accurate ohmmeter was employed to measure the sensor's resistance from the outside. Various mixtures of H_2S in synthetic air (80% nitrogen and 20% oxygen) were transferred through the closed chamber using one valve and then expelled through a second valve to maintain the pressure at 1 atm. The source of H_2S was a specialized cylinder—H2S SENSIT (Sensit Technologies LLC, Valparaiso, IN, USA)—that supplied a concentration of 25 ppm hydrogen sulfide in the air. The specific amount of H_2S in synthetic air was analyzed one sample at a time using a Gastec detection system equipped with tube no. 4 LT (Gastec Corporation, Kanagawa, Japan), which detects hydrogen sulfide within a range of 0.05 to 1 ppm. The

detection limit was 0.01 ppm, which significantly surpasses the sensor's detection limit. The resistance of the sensor—as an average of five measurements—was linked to the concentration of H_2S on the calibration curve, for a range of H_2S concentrations in the air of up to 1 ppm. The reasonable detection limit (LoD) was determined to be 0.1 ppm, as shown in Figure 15, which is a suitable value for the suggested applications for personal external clinic usage. Under this concentration level, the resistance values are making the sensor unreliable for comparison with very low gas concentrations, which are also challenging to accurately measure with the gas detector used.

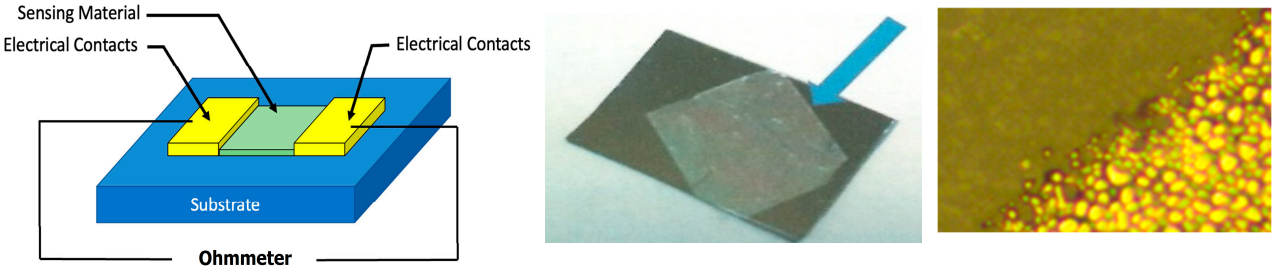


Figure 15. Sensor description: (**a**) design concept; (**b**) sensing material on SiO_2/Si substrate; (**c**) metalized electrical contact.

The experimental calibration curve for sensing H_2S is presented in Figure 16.

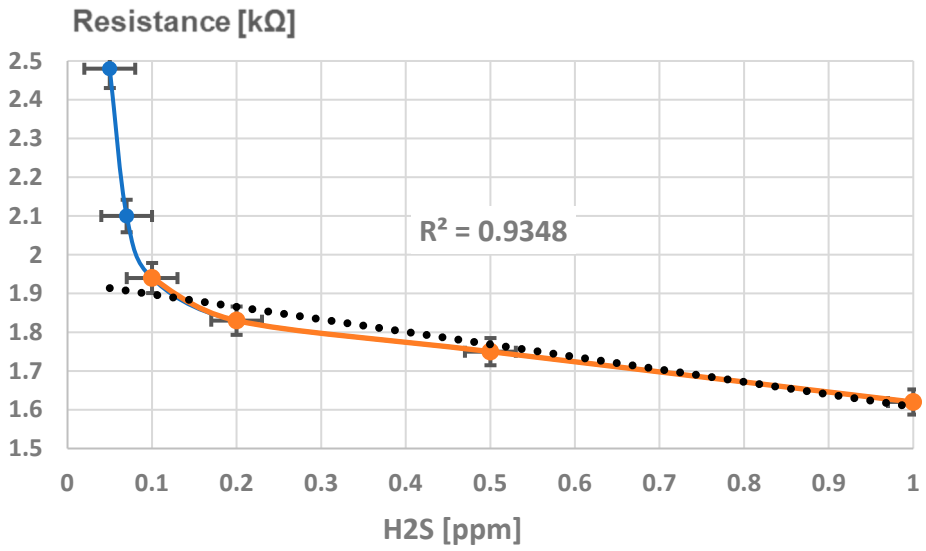


Figure 16. Experimental calibration curve with the limit of detection for sensing H_2S.

A strong correlation can be observed (R = 0.967), indicating high linearity for the domain of 0.1–1 ppm for sensing H_2S, thus making it appropriate for employing a basic signal processing system.

Figure 17 shows the variation in resistance over time for four different H_2S concentrations (0.1, 0.2, 0.5, and 1 ppm). The "On" marker indicates the beginning of measurements until the resistance attains a consistent value. "Off" denotes the condition where solely artificial air is channeled to the sensor until it attains its initial resistance level in the air. Both the decrease in resistance and the process of recovery display a quasi-exponential characteristic.

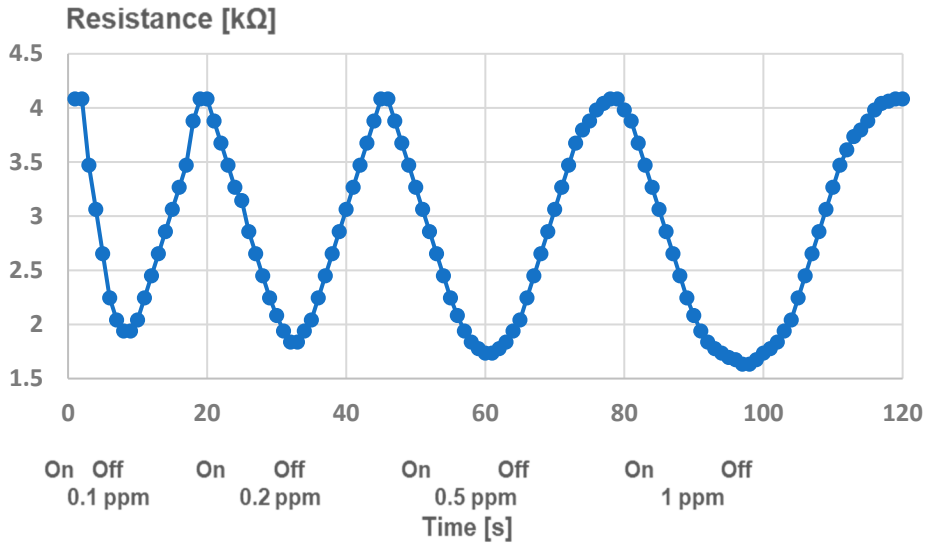


Figure 17. Experimental resistance–time curves.

Figure 18 illustrates the evaluation of the experimental response time and recovery time of the sensing structure.

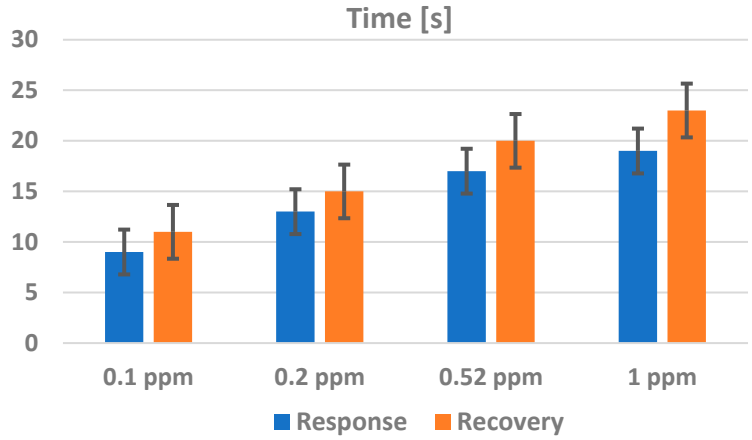


Figure 18. Experimental response and recovery time.

The response time values close to 10 s at 0.1 ppm H_2S concentration are associated with a gradually slow exhalation of air via the mouth. Concerning the recovery time value, it varies based on gas concentrations, and it is advised to go beyond 20 s for a more accurate repetitive measurement. However, it is reasonable to wait a few minutes between successive measurements for medical reasons, even if assessing several individuals with the same device.

The detection hybrid systems associated with ceramic nanotubes and conducting polymers are still of high interest, because these combinations are new, especially with the insertion of metal nanoparticles. The efficient uptake of gas molecules is key in attaining significant sensor responses, primarily attributed—particularly in hybrid assemblies—to the large grain sizes, with a high surface–volume ratios. Conversely, the semiconducting characteristics of ceramic nanotubes combined with conductive polymer assemblies, enhanced by the presence of gold nanoparticles, increases the affinity for specific gas molecules because of improved carrier transport and the synergistic interactions between the components. It is believed that incorporating metal oxide nanostructures into the polymer matrix creates a P-N heterojunction at the interfaces, at which the presence of gold nanoparticles—leading to the creation of new energy levels close to the conduction band—are essential for gas

molecule absorption at low quantities. In our specific situation, the affinity of H_2S for TiO_2 anatase is attributed to the enhancement of electronic conductivity of TiO_2 when H_2S is present, indicating a significant interaction between TiO_2 and the adsorbate, a point also emphasized in [56,57], despite these studies not focusing on sensor applications. According to the activation energy barriers, the findings suggest that anatase TiO_2 displays high reactivity towards H_2S, leading to S-substitution at the O_2c sites on the TiO_2 surface, which reduces its band gap. Moreover, when compared to other metal oxides, TiO_2 appears to provide the strongest affinity for H_2S as well [58]. The formation of vacancies combined with S on the TiO_2 surface improves the H_2S adsorption energy, a factor that is amplified in our case by the increase of TiO_2's active surface in the form of nanotubes. In [58], it was demonstrated that surpassing 200 °C can cause adsorption to result in dissociation phenomena, highlighting the strong attraction of H_2S to TiO_2. This situation is not connected to our application, but any advancements that boost the H_2S affinity for TiO_2 at room temperature are essential. Thus, the embedding of Au nanoparticles might additionally lower the band gap of the hybrid structure. Additional studies highlighted the potential benefits of, e.g., Ag decoration on TiO_2 [59], or gold-nanoparticle-decorated SnO_2 [60] for H_2S gas detection, reinforcing the significance of metal inclusions, particularly, as conducted in our research, at the nanoscale, within more complex structures.

Concerning the characteristics of the sensor introduced here for hydrogen sulfide, its capabilities are evidently better than those of similar sensors that rely only on basic various nanostructured types of TiO_2, such as [61–63]. In those instances, the detection limit is significantly higher, and the sensitivity relies on operating at increased temperatures of over 100 °C, making them unsuitable for medical purposes. A comparable analysis could be made also regarding sensors that utilize metallic nanoparticles, as seen in [64,65], but while their detection limits align with our sensors, their detection mechanism is optical, making it inappropriate for medical applications.

Recent studies introduce alternative sensor types, such as those utilizing gold nanoclusters, MXene, or metal–organic frameworks, which could potentially measure hydrogen sulfide with greater accuracy [66]. Nonetheless, while the declared optimal detection limit is claimed to be 10–30 ppb, this must be weighed against the intricate technology employed, which is quite challenging to implement on an industrial scale for medical applications.

Concerning sensors utilizing embedded gold nanoclusters within metal–organic frameworks, the latest developments for gas sensors, as outlined in [67–69], show that their detection limit for H_2S of over 10 ppm is significantly greater than that of our sensors. On the other hand, their primary use pertains to identifying allowable occupational exposure limits for H_2S in industrial settings, rather than for the diagnosis of oral diseases.

As a result of these initial successful outcomes, the characteristics of the sensor (primarily in terms of sensitivity, selectivity, response time, and reproducibility) will undergo additional examination in the context of influencing factors, also linked to the breathing process. The possible influence effects of exhaled CO_2, exhaled moisture, and possibly exhaled CH_4 will be evaluated. This research could offer further significance in linking malodor with associated digestive syndromes, a topic of great interest in the medical field.

5. Conclusions

The process of producing active surfaces for chemiresistors, based on hybrid nanostructures obtained from TiO_2 ceramic nanotubes and conducting polymers (poly(3-hexylthiophene), polyaniline emeraldine-base, and poly(3,4-ethylenedioxythiophene)-polystyrene sulfonate) with the addition of gold nanoparticles, was technologically described.

The method used to fabricate hybrid nanostructures from TiO_2 nanotubes and conducting polymers was drop-casting. Additionally, the resulting structures were immersed

in a $HAuCl_4$/2–propanol solution using an innovative dip-coating technique, and subsequently subjected to a regulated heating process from ambient temperature to slightly over one hundred degrees Celsius. The method provides a nearly uniformly dispersing of gold nanoparticles with an average dimension of 100 nm over more extensive surfaces of structures.

AFM analysis highlighted that the highest roughness was observed in the TiO_2–PANI-EB structure with Au, featuring a significantly larger grain size of over 3.5 µm and a fair symmetry in grain distribution relative to the surface. The Rku parameter values were around three, indicating that the respective grain layers mainly displayed peaks instead of depressions, exhibiting a Gaussian distribution. This configuration seems to be the most likely candidate for evaluating chemisensor characteristics, given the increased inclusion of gold and its arrangement on the surface, as well as the surface morphology.

A chemiresistor was produced using an ink-jet printer, the applied metallization being made with commercial silver ink for printed electronics. A resistor was designed with an active area of about 2 cm^2. A calibration curve was experimentally generated for the sensing structure, spanning a broader range of H_2S concentration in air, reaching up to 1 ppm, and providing a reasonable linearity. It was established that the detection limit is 0.1 ppm, a level suitable for the identification of oral diseases. The sensor can be described as a straightforward, low-cost, and robust device meant for personal use, proving to be highly advantageous at the patient level as it allows for more effective monitoring of the syndrome's progression or treatment effectiveness.

Author Contributions: Conceptualization, A.F.T., R.C.C., T.G.S. and O.D.S.; methodology, A.F.T., R.C.C. and O.D.S.; validation, R.C.C. and A.F.T.; formal analysis, A.F.T., T.G.S. and R.C.C.; investigation, R.C.C., O.D.S., T.G.S. and A.F.T.; data curation, R.C.C., O.D.S., T.G.S. and A.F.T.; writing—original draft preparation, A.F.T. and R.C.C.; writing—review and editing, R.C.C.; visualization, R.C.C., O.D.S., T.G.S. and A.F.T.; supervision, A.F.T. and R.C.C. All authors have read and agreed to the published version of the manuscript.

Funding: This research received no external funding.

Institutional Review Board Statement: Not applicable.

Informed Consent Statement: Not applicable.

Data Availability Statement: Data are contained within the article.

Conflicts of Interest: The authors declare no conflicts of interest.

References

1. Tanda, N.; Hoshikawa, Y.; Ishida, N.; Sato, T.; Takahashi, N.; Hosokawa, R.; Koseki, T. Oral malodorous gases and oral microbiota: From halitosis to carcinogenesis. *J. Oral. Biosci.* **2015**, *57*, 175–178. [CrossRef]
2. Wu, D.; Ngowi, E.; Zhai, Y.; Wang, Y.; Khan, N.; Kombo, A.; Khattak, S.; Li, T.; Ji, R. Role of Hydrogen Sulfide in Oral Disease. *Oxid. Med. Cell Longev.* **2022**, *25*, 1886277. [CrossRef]
3. Yoneda, M.; Suzuki, N.; Hirofuji, T. Current Status of the Techniques Used for Halitosis Analysis. *Austin Chromatogr.* **2015**, *2*, 1024.
4. Lee, Y.; Shin, S.; Hong, J. Investigation of volatile sulfur compound level and halitosis in patients with gingivitis and periodontitis. *Sci. Rep.* **2023**, *13*, 13175. [CrossRef] [PubMed]
5. Available online: https://www.breathinstitute.co.uk/medical-library-bad-breath/methods-of-diagnosis-and-causes-of-bad-breath/breath-gas-measurement-methods/ (accessed on 18 December 2024).
6. Nakhleh, M.K.; Quatredeniers, M.; Haick, H. Detection of Halitosis in Breath: Between the Past, Present and Future. *Oral Dis.* **2017**, *24*, 685–695. [CrossRef]
7. Available online: https://www.glsciencesinc.com/oralchroma?srsltid=AfmBOooEzSxQkIdBPg5LPXkIQN8xrjUGIM8hVsLnPX13nm0qTWZXdUXJ (accessed on 18 December 2024).
8. Available online: https://www.halimeter.com/ (accessed on 18 December 2024).

9. Salako, N.; Philip, L. Comparison of the use of the Halimeter and the Oral Chroma™ in the assessment of the ability of common cultivable oral anaerobic bacteria to produce malodorous volatile sulfur compounds from cysteine and methionine. *Med. Princ. Pract.* **2011**, *20*, 75. [CrossRef]
10. Hanada, M.; Koda, H.; Onaga, K.; Tanaka, K.; Okabayashi, T.; Itoh, T.; Miyazaki, H. Portable oral malodor analyzer using highly sensitive In_2O_3 gas sensor combined with a simple gas chromatography system. *Analytica Chimica Acta* **2003**, *475*, 27–35. [CrossRef]
11. Ikava, K.; Iwakura, M.; Washio, J.; Kusano, A.; Tanda, N.; Koseki, T. Circadian changes of volatile sulfur compounds measured by Breathtron™. *Int. Congr. Ser.* **2005**, *1284*, 89–90. [CrossRef]
12. Zhang, T.; Xue, Y.; Chen, Y.; Wan, H.; Wang, P. Research on Intelligent Electronic Nose Based on Exhaled Breath to Detect Halitosis. *ECS Meet. Abstr.* **2021**, *MA 2021-01*, 1348. [CrossRef]
13. Umapathy, V.; Natarajan, P.; Swamikannu, B.; Moses, J.; Jones, S.; Chandran, M.; Anbumozhi, M. Emerging Biosensors for Oral Cancer Detection and Diagnosis—A Review Unravelling Their Role in Past and Present Advancements in the Field of Early Diagnosis. *Biosensors* **2022**, *12*, 498. [CrossRef]
14. Li, Y.; Tang, H.; Liu, Y.; Qiao, Y.; Xia, H.; Zhou, J. Oral wearable sensors: Health management based on the oral cavity. *Biosens. Bioelectron.* **2022**, *10*, 100135. [CrossRef]
15. *EP0819940A2*; Method of Detecting Halitosis and Detector for Use in the Method. European Patent Office: Munich, Germany, 1997.
16. Dey, A. Semiconductor metal oxide gas sensors: A review. *Mater. Sci. Eng. B Solid-State Mater. Adv. Technol.* **2018**, *229*, 206–217. [CrossRef]
17. Wang, T.; Sun, P.; Liu, F.; Lu, G. Revealing the correlation between gas selectivity and semiconductor energy band structure derived from off-stoichiometric spinel $CdGa_2O_4$. *Sens. Actuators B* **2022**, *352*, 131039. [CrossRef]
18. He, H.; Zhao, C.; Xu, J.; Qu, K.; Jiang, Z.; Gao, Z.; Song, Y. Exploiting Free-Standing p-CuO/n-TiO_2 Nanochannels as a Flexible Gas Sensor with High Sensitivity for H_2S at Room Temperature. *ACS Sens.* **2021**, *6*, 3387–3397. [CrossRef] [PubMed]
19. Li, Z.; Wang, N.; Lin, Z.; Wang, J.; Liu, W.; Sun, K.; Fu, Y.; Wang, Z. Room-Temperature High-Performance H_2S Sensor Based on Porous CuO Nanosheets Prepared by Hydrothermal Method. *ACS Appl. Mater. Interfaces* **2016**, *8*, 20962–20968. [CrossRef]
20. Han, G.; Liu, C.; Guan, C.; Li, I.; Wang, Y.; Li, Z. Advances in electrochemical biosensors for the detection of common oral diseases. *Authorea.* **2023**. [CrossRef]
21. Se, A.; Albarella, J.; Carey, J.; Kim, P.; McNamara, W. Low-cost colorimetric sensor for the quantitative detection of gaseous hydrogen sulfide. *Sens. Actuators B Chem.* **2008**, *134*, 234–237. [CrossRef]
22. Lu, Y.; Wang, D.; Lv, W.; Xia, Y.; Ou, K.; Li, Y.; Du, Z.; He, Y.; Dai, J.; Wu, S.; et al. Surface acoustic wave hydrogen sulfide gas sensors based on porous SnO_2-SiO_2 composite films. *Sens. Actuators B Chem.* **2024**, *417*, 136117. [CrossRef]
23. Zhao, L.; Che, J.; Cao, Q.; Shen, S.; Tang, Y. Highly Sensitive Surface Acoustic Wave H_2S Gas Sensor Using Electron-beam-evaporated CuO as Sensitive Layer. *Sens. Mater.* **2023**, *35*, 2293–2304. Available online: https://sensors.myu-group.co.jp/sm_pdf/SM3323.pdf (accessed on 18 December 2024). [CrossRef]
24. Ohatkar, S.; Rane, S.; Ambesange, A.; More, A.; Rane, S. Nanostructured Metal Oxide Based Thick Film Sensors. *Int. J. Latest Technol. Eng. Manag. Appl. Sci.* **2016**, *5*, 93–97. Available online: https://www.ijltemas.in/DigitalLibrary/Vol.5Issue5/93-97.pdf (accessed on 18 December 2024).
25. Ayyala, S.; Covington, J. Nickel-Oxide Based Thick-Film Gas Sensors for Volatile Organic Compound Detection. *Chemosensors* **2021**, *9*, 247. [CrossRef]
26. Shin, H.; Kim, D.; Jung, W.; Jang, J.; Kim, Y.; Lee, Y.; Chang, K.; Lee, J.; Park, J.; Namkoong, K.; et al. Surface Activity-Tuned Metal Oxide Chemiresistor: Toward Direct and Quantitative Halitosis Diagnosis. *ACS Nano* **2021**, *15*, 9. [CrossRef]
27. Wang, C.; Jiang, L.; Wang, J.; Liu, F.; You, R.; Lv, S.; Yang, Z.; He, J.; Liu, A.; Yan, X.; et al. Mixed potential type H_2S sensor based on stabilized zirconia and a Co_2SnO_4 sensing electrode for halitosis monitoring. *Sens. Actuators B Chem.* **2020**, *321*, 128587. [CrossRef]
28. Ma, S.; Jia, J.; Tian, Y.; Cao, L.; Shi, S.; Li, X.; Wang, Z. Improved H_2S sensing properties of Ag/TiO_2 nanofibers. *Ceram. Int.* **2016**, *42*, 2041.
29. Shirsat, M.; Bangar, M.; Deshusses, M.; Myung, N.; Mulchandani, A. Polyaniline nanowires-gold nanoparticles hybrid network based chemiresistive hydrogen sulfide sensor. *Appl. Phys. Lett.* **2009**, *94*, 083502. [CrossRef]
30. Feng, D.; Du, L.; Xing, X.; Wang, C.; Chen, J.; Zhu, Z.; Tian, Y.; Yang, D. Highly Sensitive and Selective NiO/WO_3 Composite Nanoparticles in Detecting H_2S Biomarker of Halitosis. *ACS Sens.* **2021**, *6*, 733–741. [CrossRef]
31. Panes-Ruiz, L.; Riemenschneider, L.; Chawa, M.; Loffler, M.; Rellinghaus, B.; Tetzlaff, R.; Bezugly, V.; Ibarlucea, B.; Cuniberti, G. Selective and self-validating breath-level detection of hydrogen sulfide in humid air by gold nanoparticle-functionalized nanotube arrays. *Nano Res.* **2022**, *15*, 2512–2521. [CrossRef]
32. Kato, T.; Tanaka, T.; Uchida, K. Detection of PPB-Level H_2S Concentrations in Exhaled Breath Using Au Nanosheet Sensors with Small Variability, High Selectivity, and Long-Term Stability. *ACS Sens.* **2024**, *9*, 708–716. [CrossRef]

33. Ramgir, N.; Sharma, P.; Datta, N.; Kaur, M.; Debnath, A.; Aswal, D.; Gupta, S. Room temperature H_2S sensor based on Au modified ZnO nanowires. *Sens. Actuators B Chem.* **2013**, *186*, 718–726. [CrossRef]
34. Kaiser, A.; Ceja, E.; Huber, F.; Herr, U.; Thonke, K. Highly Sensitive H_2S Sensing with Gold and Platinum Surface-Modified ZnO Nanowire ChemFETs. *Proceedings* **2020**, *60*, 7. [CrossRef]
35. Vuong, N.; Kim, D.; Kim, H. Porous Au-embedded WO3 Nanowire Structure for Efficient Detection of CH_4 and H_2S. *Sci. Rep.* **2015**, *5*, 11040. Available online: https://www.nature.com/articles/srep11040 (accessed on 18 December 2024).
36. Punginsang, M.; Liewhiran, C.; Wisitsoraat, A.; Zappa, D.; Comini, E.; Sberveglieri, G. Selective H_2S Gas Sensors Based on Au-functionalized WO_3 Nanowires. In Proceedings of the 17th International Meeting on Chemical Sensors—IMCS 2018, Vienna, Austria, 15–19 July 2018; pp. 853–854. [CrossRef]
37. Hitchman, M.; Saffell, J. Considerations of Thermodynamics and Kinetics for the Effects of Relative Humidity on the Electrolyte in Electrochemical Toxic Gas Sensors. *ACS Sens.* **2021**, *6*, 3985–3993. [CrossRef]
38. Xu, Q.; Zong, B.; Li, Q.; Fang, X.; Mao, S.; Ostrikov, K. H_2S sensing under various humidity conditions with Ag nanoparticle functionalized $Ti_3C_2T_x$ MXene field-effect transistors. *J. Hazard. Mater.* **2022**, *424*, 127492. [CrossRef] [PubMed]
39. Deng, Z.; Wu, Z.; Liu, X.; Chen, Z.; Sun, Y.; Dai, N.; Ge, M. Humidity-tolerant and highly sensitive gas sensor for hydrogen sulfide based on WO_3 nanocubes modified with CeO_2. *RSC Adv.* **2024**, *14*, 15039–15047. [CrossRef]
40. Enculescu, M.; Costas, A.; Evanghelidis, A.; Enculescu, I. Fabrication of ZnO and TiO_2 Nanotubes via Flexible Electrospun Nanofibers for Photocatalytic Applications. *Nanomaterials* **2021**, *11*, 1305. [CrossRef] [PubMed]
41. Trandabat, A.F.; Ciobanu, R.C.; Schreiner, O.D.; Aradoaei, M.; Aradoaei, S. Manufacturing of TiO_2, Al_2O_3 and Y_2O_3 Ceramic Nanotubes for Application as Electrodes for Printable Electrochemical Sensors. *Crystals* **2024**, *14*, 454. [CrossRef]
42. Trandabat, A.F.; Ciobanu, R.C.; Schreiner, O.D.; Schreiner, T.G.; Aradoaei, S. Ceramic Nanotubes—Conducting Polymer Assemblies with Potential Application as Chemosensors for Breath Hydrogen sulfide Detection in Chronic Kidney Disease. *Chemosensors* **2024**, *12*, 198. [CrossRef]
43. Umeda, H.; Mezaki, Y.; Oshio, A.; Kaneko, Y.; Okamoto, R.; Kusumoto, S.; Kunimura, S. Gold Nanoparticles Produced by Low-temperature Heating of the Dry Residue of a Droplet of an HCl Acidic Solution of $HAuCl_4{\cdot}4H_2O$ in a Low Vacuum. *Anal. Sci.* **2021**, *37*, 1427–1432. [CrossRef]
44. Ii, K.; Kurita, Y.; Kida, N.; Kunimura, S. Preparation of gold nanoparticles using low-temperature heating of the dry residue of a droplet of an $HAuCl_4$ solution in air. *Anal. Sci.* **2024**, *40*, 213–217. [CrossRef]
45. Surface Roughness Parameters. Available online: https://www.keyence.eu/ss/products/microscope/roughness/line/tab03_b.jsp (accessed on 18 December 2024).
46. *ISO 21920-2:2021*; Geometrical Product specifications (GPS)—Surface Texture: Profile. ISO: Geneva, Switzerland. Available online: https://www.iso.org/standard/72226.html (accessed on 18 December 2024).
47. Taudul, B.; Tielens, F.; Calatayud, M. On the Origin of Raman Activity in Anatase TiO_2 (Nano)Materials: An Ab Initio Investigation of Surface and Size Effects. *Nanomaterials* **2023**, *13*, 1856. [CrossRef]
48. Quillard, S.; Louarn, G.; Lefrant, S.; Macdiarmid, A.G. Vibrational analysis of polyaniline: A comparative study of leucoemeraldine, emeraldine, and pernigraniline bases. *Phys. Rev. B* **1994**, *50*, 12496.
49. Garreau, S.; Louarn, G.; Buisson, J.P.; Froyer, G.; Lefrant, S. In Situ Spectroelectrochemical Raman Studies of Poly(3,4-ethylenedioxythiophene) (PEDT). *Macromolecules* **1999**, *32*, 6807–6812.
50. Trznadel, M.; Zagórska, M.; Lapkowski, M.; Louarn, G.; Lefrant, S.; Pron, A. UV–VIS–NIR and Raman spectroelectrochemistry of regioregular poly(3-octylthiophene): Comparison with its non-regioregular analogue. *J. Chem. Soc. Faraday Trans.* **1998**, *24*, 3527–3780.
51. Santos, E.; Catto, E.; Peterline, A.; Avansi, W. Transition metal (Nb and W) doped TiO_2 nanostructures: The role of metal doping in their photocatalytic activity and ozone gas-sensing performance. *Appl. Surf. Sci.* **2022**, *579*, 152146. [CrossRef]
52. Orizu, G.; Ugwuoke, P.; Asogwa, P.; Offiah, S. A review on the inference of doping TiO_2 with metals/nonmetals to improve its photocatalytic activities. *IOP Conf. Ser. Earth Environ. Sci.* **2023**, *1178*, 012008. [CrossRef]
53. Gartner, M.; Szekeres, A.; Stroescu, H.; Mitrea, D.; Covei, M. Advanced Nanostructured Coatings Based on Doped TiO_2 for Various Applications. *Molecules* **2023**, *28*, 7828. [CrossRef] [PubMed]
54. McGarrity, M.; Zhao, F. Graphene-Based Chemiresistor Sensors for Drinking Water Quality Monitoring. *Sensors* **2023**, *23*, 9828. [CrossRef]
55. Lin, Y.; Manalili, D.; Khodabakhsh, A.; Cristescu, S.M. Real-Time Measurement of CH_4 in Human Breath Using a Compact CH_4/CO_2 Sensor. *Sensors* **2024**, *24*, 1077. [CrossRef]
56. Yanxin, C.; Yi, J.; Wenzhao, L.; Rongchao, J.; Shaozhen, T.; Wenbin, H. Adsorption and interaction of H_2S/SO_2 on TiO_2. *Catal. Today* **1999**, *50*, 39–47. [CrossRef]
57. Junkaew, A.; Maitarad, P.; Arróyave, R.; Kungwan, N.; Zhang, D.; Shib, L.; Namuangruk, S. The complete reaction mechanism of H_2S desulfurization on an anatase TiO_2 (001) surface: A density functional theory investigation. *Catal. Sci. Technol.* **2017**, *7*, 356–365. [CrossRef]

58. Shahzad, N.; Hussain, A.; Mustafa, N.; Ali, N.; Kanounf, M.; Goumri-Said, S. First principles study of the adsorption and dissociation mechanisms of H_2S on a TiO_2 anatase (001) surface. *RSC Adv.* **2016**, *6*, 7941–7949. [CrossRef]
59. Hwang, J.; Kim, M.; Jin, C.; Mirzaei, A.; Choi, S.; Choi, M.; Lee, H. Surface Reaction Mechanism and Characteristics of 2-Dimensional TiO_2 and 0-Dimensional Ag Nanocomposites Specialized for H_2S Gas Sensing at Room Temperature. *Sens. Actuators Rep.* **2025**, *9*, 100290. [CrossRef]
60. Rodiawan; Wang, S.; Suhdi. Gold-nanoparticle-decorated Tin Oxide of a Gas Sensor Material for Detecting Low Concentrations of Hydrogen Sulfide. *Sens. Mater.* **2023**, *35*, 1121–1130. [CrossRef]
61. Nagmani; Pravarthana, D.; Tyagi, A.; Jagadale, T.C.; Prellier, W.; Aswal, D.K. Highly sensitive and selective H_2S gas sensor based on TiO_2 thin films. *Appl. Surf. Sci.* **2021**, *549*, 149281. [CrossRef]
62. Alaya, I.; Madani, M.; Bouguila, N.; El Mir, L.; Fazio, E.; Corsaro, C.; Neri, G. Conductometric H_2S Sensors Based on TiO_2 Nanoparticles. *Materials* **2024**, *17*, 3283. [CrossRef] [PubMed]
63. Tong, X.; Shen, W.; Chen, X.; Corriou, J. A fast response and recovery H_2S gas sensor based on free-standing TiO_2 nanotube array films prepared by one-step anodization method. *Ceram. Int.* **2017**, *43*, 14200–14209. [CrossRef]
64. Marquardt, N.; Dahlke, M.; Schaate, A. Cu-MOF-808 as a Sensing Material for Gaseous Hydrogen Sulfide. *ChemPlusChem* **2023**, *88*, e202300109. [CrossRef]
65. Yu, Q.; Gao, P.; Zhang, K.; Tong, X.; Yang, H.; Liu, S.; Du, J.; Zhao, Q.; Huang, W. Luminescent gold nanocluster-based sensing platform for accurate H_2S detection in vitro and in vivo with improved anti-interference. *Light Sci. Appl.* **2017**, *6*, e17107. [CrossRef]
66. Yang, M.; Zhou, Y.; Wang, K.; Luo, C.; Xie, M.; Shi, X.; Lin, X. Review of Chemical Sensors for Hydrogen Sulfide Detection in Organisms and Living Cells. *Sensors* **2023**, *23*, 3316. [CrossRef]
67. Nie, X.; Han, X.; Yu, S.; Liu, W.; Yang, Y. Embedding gold nanoclusters in metal-organic frameworks as a dual-channel hydrogel optical sensor for hydrogen sulfide detection. *J. Solid State Chem.* **2025**, *346*, 125283. [CrossRef]
68. Wang, Z.J.; Li, Q.; Tan, L.L.; Liu, C.; Shang, L. Metal–Organic Frameworks-Mediated Assembly of Gold Nanoclusters for Sensing Applications. *J. Anal. Test.* **2022**, *6*, 163–177. [CrossRef] [PubMed]
69. Ali, A.; Alzamly, A.; Greish, Y.; Bakiro, M.; Nguyen, H.; Mahmoud, S. A Highly Sensitive and Flexible Metal–Organic Framework Polymer-Based H_2S Gas Sensor. *ACS Omega* **2021**, *6*, 17690–17697. [CrossRef] [PubMed]

Disclaimer/Publisher's Note: The statements, opinions and data contained in all publications are solely those of the individual author(s) and contributor(s) and not of MDPI and/or the editor(s). MDPI and/or the editor(s) disclaim responsibility for any injury to people or property resulting from any ideas, methods, instructions or products referred to in the content.